A simple and exact acoustic wavefield modelling code for data processing, imaging and interferometry applications

Erica Galetti*, David Halliday†, and Andrew Curtis*

**School of GeoSciences, University of Edinburgh, Grant Institute, King's Buildings, West Mains Road, Edinburgh EH9 3JW, United Kingdom. E-mail: erica.galetti@ed.ac.uk; Andrew.Curtis@ed.ac.uk. † Schlumberger Gould Research, High Cross, Madingley Road, Cambridge CB3 0EL, United Kingdom. E-mail: dhalliday@slb.com.*

(March 5, 2013)

Running head: **Exact modelling in scattering media**

ABSTRACT

Improvements in industrial seismic, seismological, acoustic or interferometric theory and applications often result in quite subtle changes in sound quality, seismic images or information which are nevertheless crucial for improved interpretation or experience. When evaluating new theories and algorithms using synthetic data, an important aspect of related research is therefore that numerical errors due to wavefield modelling are reduced to a minimum. We present a new MATLAB code based on the Foldy method that models theoretically exact direct and scattered parts of a wavefield. Its main advantage lies in the fact that, while all multiple scattering interactions are taken into account, unlike finite-difference or finite-element methods, numerical dispersion errors are avoided. The method is therefore ideal for testing new theory in industrial seismics, seismology, acoustics and in wavefield interferometry in particular since the latter is particularly sensitive to the dynamics of scattering interactions. We present the theory behind the Foldy acoustic modelling method

and provide examples of its implementation. We also benchmark the code against a good finite-difference code. As our Foldy code was written and optimized to test new theory in seismic interferometry, a number of examples of its application to seismic interferometry are also presented, showing its validity and importance when exact modelling results are needed.

INTRODUCTION

Testing new algorithms in acoustics or exploration and earthquake seismology normally requires a synthetic dataset to be created in order to assess the validity of the theory on virtually error-free data. A number of wavefield modelling methods and codes are currently available, allowing variously for different levels of complexity in the velocity model, and providing different levels of accuracy in the construction of direct and multiply-scattered events. Among the most popular modelling techniques, numerical grid-based schemes such as finite-differences, finite-elements and pseudospectral methods are possibly the most commonly used, enabling the user to model realistic signals or seismograms for either acoustic or elastic wave propagation through media of any desired degree of complexity. These numerical methods use 2- or 3-D grids of points to track the evolution of the wavefield in a medium by approximating the time and space derivatives of the equations of motion. As both the medium and the equations are discretised, the accuracy of the results can be improved by decreasing the grid size and increasing the order of derivative approximations, at the expense of memory usage and computation time. Using coarser grids and lower-order derivatives reduces that computational burden, but can introduce numerical errors that may spread throughout any subsequent operation that is performed on the modelled data. In addition, numerical errors may be introduced by linear interpolation between staggered grid cells and by the model having finite dimensions and artificial boundaries, which constrain the size of the velocity grid (and the number of computations required), and which often produce non-physical reflections off the sides of the model in the absence of absolute energy absorption methods at the boundaries.

Given that a compromise between accuracy and computational power is always necessary

in practice, when testing the reliability of any data processing or interpretation algorithm it may not be possible to assess whether errors in the results are the product of incorrect theory in the algorithm, or simply arise from the modelling method used. In such cases, a simple, fast and exact modelling scheme is extremely useful in order to reduce the impact of modelling errors on the results and eliminate numerical dispersion from the range of possible causes of errors in the results.

In this article, we present an exact method for acoustic modelling of direct and scattered wavefields that uses the theory of multiple scattering (or diffraction) developed by Foldy (1945). Although we do not introduce new scientific concepts herein, we bring together existing theory to produce a modelling code that is exact and can easily be adapted and applied when testing new algorithms in acoustics, seismic imaging, seismology and wavefield interferometry. We give examples of the latter here and in the code package.

The code, written in MATLAB, uses multiple scattering theory to model the acoustic wavefield produced by monopole or dipole (spatial derivative) sources as it propagates through a scattering medium and is recorded by monopole or dipole receivers. Monopole impulse-responses are calculated in the frequency domain using the analytical Green's function formulae from Snieder (2009), with the option of adding a Ricker wavelet to the source. Dipole (derivative) Green's functions are also evaluated analytically from the frequency-domain spatial derivative of the monopole Green's functions. The Foldy method uses analytic solutions to the wave equation (Green's functions) to propagate energy through the non-scattering background medium. As analytic Green's function formulae exist in various numbers of dimensions, the code can easily perform 1-, 2- or 3-D modelling by simply choosing the appropriate formula (all of these are included). A practical limitation of this analytical approach is that the Foldy method and code can only model direct and scat-

tered wavefields in a homogeneous medium of uniform velocity. However, this prevents any numerical error due to ray tracing from propagating across the dataset and allows the modelling results to be exact and free from numerical errors (to machine precision).

The scattered part of the wavefield is modelled by including isotropic point-scatterers (i.e., diffractors that scatter spherically symmetrical waves in the 3D case) in the medium, and computing all possible interactions between them by using an exact solution to the infinite scattering series. Although such infinitely small point-scatterers do not exist in reality, they represent the scattering process while avoiding the introduction of any errors that would be produced if the diffractors had a finite size and physical properties. They can also be used to model more continuous structures like reflectors by placing them close together in a line and, because a relationship exists between wavelength and scatterer cross-section (Foldy, 1945; Snieder, 1988a,b; Groenenboom and Snieder, 1995), point-scatterers may be used to approximate real scattering bodies.

Although the Foldy modelling method is not intended to substitute for the more advanced grid-based modelling schemes for practical applications, it is nevertheless a powerful tool in the acoustician's and geophysicist's arsenals: because it is exact and theoretically error-free, it can be used safely to assess the validity of data processing, imaging and interferometry algorithms, and thus to detect any errors in the theory, before moving on to more complicated and realistic cases that require grid-based modelling methods, and real data tests and applications.

Within this paper, we first describe the theory of multiple scattering as developed by Foldy (1945). As the code was created to test new theory in seismic interferometry (and will be useful to others who develop and test interferometry algorithms in future), we then

give a brief overview of interferometric theory, and illustrate the application of the code in a number of examples. Finally, we discuss the advantages and limitations of the Foldy method in comparison with grid-based modelling methods such as finite-differences. The monopole and dipole Green's function formulae that are used in the code are provided in Appendix A.

THE FOLDY METHOD

Consider a source and a receiver respectively located at position $\mathbf{x}_S$ and $\mathbf{x}_R$ within a homogeneous medium containing a distribution of N scatterers. The total wavefield $\Psi(\mathbf{x}_R)$ recorded at $\mathbf{x}_R$ from the source at $\mathbf{x}_S$ is given by the sum of the direct and scattered wavefield: while the former can easily be calculated as a Green's function from the source to the receiver, the computation of the latter is more complicated as it requires the evaluation of the direct wavefield to each scatterer, wavefield scattering or diffraction, and all possible multiple-scattering interactions of that scattered field. Together these provide the total wavefield radiated by each single scatterer (Figure 1). The total wavefield reaching the receiver is finally obtained by summing the components of the wavefield radiated by each scatterer which then propagate to the receiver location.

By assuming the diffractors are limited to isotropic point scatterers we can reduce the multiple scattering process to a system of linear equations which can be solved numerically (Foldy, 1945; Groenenboom and Snieder, 1995). In the frequency domain, the total wavefield $\Psi(\mathbf{x}_R)$ can be expressed as follows:

$$\Psi(\mathbf{x}_R) = \Psi_0(\mathbf{x}_R) + \sum_{i=1}^{N} \Psi(\mathbf{x}^{(i)}) A^{(i)} G(\mathbf{x}_R, \mathbf{x}^{(i)}) \; . \tag{1}$$

Here $\Psi_0(\mathbf{x}_R)$ denotes the direct wavefield from $\mathbf{x}_S$ to $\mathbf{x}_R$, $\Psi(\mathbf{x}^{(i)})$ denotes the total wavefield

(direct and scattered) reaching scatterer (i) located at $\mathbf{x}^{(i)}$, $A^{(i)}$ is the scattering amplitude of scatterer (i), and $G(\mathbf{x}_R, \mathbf{x}^{(i)})$ is the full Green's function between scatterer (i) and receiver $\mathbf{x}_R$. Also, when the wavefield emitted by the source at $\mathbf{x}_S$ is simply a Green's function convolved with a source wavelet $s(\omega)$, the direct wavefield $\Psi_0(\mathbf{x}_R)$ can be expressed as

$$\Psi_0(\mathbf{x}_R) = s(\omega)G(\mathbf{x}_R, \mathbf{x}_S) \ , \tag{2}$$

where $G(\mathbf{x}_R, \mathbf{x}_S)$ denotes the full Green's function between source $\mathbf{x}_S$ and receiver $\mathbf{x}_R$.

The scattering amplitude A is a complex number whose real and imaginary components can be determined from the optical theorem following principles of energy conservation. Within our code, we assume energy loss within the medium is only due to the scattering process and ignore the effects of anelastic attenuation. In order to satisfy the requirement of energy conservation, the real and imaginary parts of A are intimately related, and the value of the imaginary component must fall within a specific range - a detailed discussion on this topic is given in Appendix B.

The sum in equation 1 essentially means that any scattered wave arriving at $\mathbf{x}_R$ must have come from one of the N scatterers; hence it must have arrived at the scatterer $(\Psi(\mathbf{x}^{(i)}))$, been scattered (amplitude and phase scaled by $A^{(i)}$), and must then have propagated to the receiver $(G(\mathbf{x}_R, \mathbf{x}^{(i)}))$. The entire series of multiple scattering interactions is therefore included intrinsically within term $\Psi(\mathbf{x}^{(i)})$.

By the same reasoning, the total wavefield $\Psi(\mathbf{x}^{(i)})$ reaching scatterer (i) can be expressed as the sum of the direct and scattered wavefield, where the latter must have been scattered from any and all of the *other* scatterers:

$$\Psi(\mathbf{x}^{(i)}) = \Psi_0(\mathbf{x}^{(i)}) + \sum_{\substack{j=1 \\ j \neq i}}^{N} \Psi(\mathbf{x}^{(j)}) A^{(j)} G(\mathbf{x}^{(i)}, \mathbf{x}^{(j)}) \ , \tag{3}$$

where $\Psi_0(\mathbf{x}^{(i)})$ is the direct wavefield from $\mathbf{x}_S$ to scatterer (i), $\Psi(\mathbf{x}^{(j)})$ denotes the total wavefield reaching scatterer (j) located at $\mathbf{x}^{(j)}$, $A^{(j)}$ is the scattering amplitude of scatterer (j), and $G(\mathbf{x}^{(i)}, \mathbf{x}^{(j)})$ is the full Green's function between $\mathbf{x}^{(j)}$ and $\mathbf{x}^{(i)}$.

By swapping the order of terms, expressing the wavefields $\Psi(\mathbf{x}^{(i)})$ and $\Psi_0(\mathbf{x}^{(i)})$ as vectors, and arranging the terms $A^{(j)}G(\mathbf{x}^{(i)}, \mathbf{x}^{(j)})$ into a square matrix of dimension equal to the number of scatterers, equation 3 can be re-written as

$$\begin{pmatrix} \Psi_0(\mathbf{x}^{(1)}) \\ \Psi_0(\mathbf{x}^{(2)}) \\ \dots \\ \Psi_0(\mathbf{x}^{(N)}) \end{pmatrix} = - \begin{pmatrix} -1 & A^{(2)}G(\mathbf{x}^{(1)}, \mathbf{x}^{(2)}) & \dots & A^{(N)}G(\mathbf{x}^{(1)}, \mathbf{x}^{(N)}) \\ A^{(1)}G(\mathbf{x}^{(2)}, \mathbf{x}^{(1)}) & -1 & \dots & A^{(N)}G(\mathbf{x}^{(2)}, \mathbf{x}^{(N)}) \\ \dots & \dots & \dots & \dots \\ A^{(1)}G(\mathbf{x}^{(N)}, \mathbf{x}^{(1)}) & A^{(2)}G(\mathbf{x}^{(N)}, \mathbf{x}^{(2)}) & \dots & -1 \end{pmatrix} \begin{pmatrix} \Psi(\mathbf{x}^{(1)}) \\ \Psi(\mathbf{x}^{(2)}) \\ \dots \\ \Psi(\mathbf{x}^{(N)}) \end{pmatrix} , \tag{4}$$

where the term on the left-hand side is defined to be a vector $\mathbf{\Psi_0}$ containing the direct wavefields from the source at $\mathbf{x}_S$ to each scatterer, the first term on the right-hand side is matrix $\mathbf{M}$ containing the interaction terms between all scatterers, and the second term on the right-hand side is vector $\mathbf{\Psi}$ containing the total wavefields arriving at each scatterer. In compact form, this equation thus becomes

$$\mathbf{\Psi_0} = -\mathbf{M}\mathbf{\Psi} \, , \tag{5}$$

and since both $\mathbf{\Psi_0}$ and $\mathbf{M}$ can be calculated using equation 2 and the Green's function

formulae in Appendix A, equation 5 can be solved numerically by matrix inversion:

$$\mathbf{\Psi} = -\mathbf{M}^{-1}\mathbf{\Psi_0} \, . \tag{6}$$

Equation 6 gives a vector containing the total field that reaches each scatterer. When inserted into equation 1, this term can therefore be used to evaluate the total field that reaches the receiver at $\mathbf{x}_R$.

The equations above thus provide an exact representation of the monopole wavefield through a scattering medium of constant background velocity produced by an impulsive source at $\mathbf{x}_S$ and recorded by a receiver at $\mathbf{x}_R$, including all orders of interactions between the scatterers. The only possible sources of inaccuracy in practice are numerical, due to the finite word storage length of a real number, and any approximation in the matrix inversion in equation 6. The inverse problem in equation 6 is solved in MATLAB using the `mldivide` operation, which seeks a solution by performing a general triangular factorisation that uses LU decomposition of $\mathbf{M}$ with partial pivoting (MathWorks, 2012). If matrix $\mathbf{M}$ is singular, the solution to equation 6 either does not exist or it is non-unique. In all of our experiments, the inverse problem in equation 6 was always well-posed. In the case of dipole (derivative) sources and receivers, as used for example in acoustic time-reversal (Cassereau and Fink, 1993; Fink and Prada, 2001; Fink, 2006), in wavefield extrapolation (Berkhout and Wapenaar, 1989; Wapenaar, 1993), in seismic interferometry (Wapenaar, 2004; van Manen et al., 2005, 2006; Wapenaar and Fokkema, 2006), or in some cases in seismic acquisition (Moldoveanu et al., 2007) or imaging (Halliday and Curtis, 2010; Vasconcelos et al., 2009, 2010), equations 1-3 need to be slightly modified to take into account whether differentiation is performed at the source (to obtain a dipole source) or at the receiver (to obtain a dipole receiver). When dipole sources or receivers are used, the direct wavefield in equation 2

becomes

$$\begin{aligned}\Psi_0'(\mathbf{x}_R) &= \partial_m \Psi_0(\mathbf{x}_R) \\ &= s(\omega)\partial_m G(\mathbf{x}_R, \mathbf{x}_S) \ ,\end{aligned} \tag{7}$$

where $\partial_m G(\mathbf{x}_R, \mathbf{x}_S)$ is the partial derivative of the Green's function between source $\mathbf{x}_S$ and receiver $\mathbf{x}_R$ along the m-direction, evaluated at $\mathbf{x}_S$ for a dipole source and at $\mathbf{x}_R$ for a dipole receiver.

When differentiation is performed with respect to sources, from equation 3 we get

$$\Psi'(\mathbf{x}^{(i)}) = \Psi_0'(\mathbf{x}^{(i)}) + \sum_{\substack{j=1 \\ j\neq i}}^{N} \Psi'(\mathbf{x}^{(j)}) A^{(j)} G(\mathbf{x}^{(i)}, \mathbf{x}^{(j)}) \ , \tag{8}$$

where $\Psi_0'(\mathbf{x}^{(i)})$ is the direct dipole-source wavefield to scatterer (i). The total dipole-source wavefield recorded by receiver $\mathbf{x}_R$ is given by

$$\Psi'(\mathbf{x}_R) = \Psi_0'(\mathbf{x}_R) + \sum_{i=1}^{N} \Psi'(\mathbf{x}^{(i)}) A^{(i)} G(\mathbf{x}_R, \mathbf{x}^{(i)}) \ . \tag{9}$$

When differentiation is performed with respect to receivers, the total wavefield recorded by a dipole receiver at $\mathbf{x}_R$ is simply given by:

$$\Psi'(\mathbf{x}_R) = \Psi_0'(\mathbf{x}_R) + \sum_{i=1}^{N} \Psi(\mathbf{x}^{(i)}) A^{(i)} \partial_m G(\mathbf{x}_R, \mathbf{x}^{(i)}) \ , \tag{10}$$

where $\partial_m G(\mathbf{x}_R, \mathbf{x}^{(i)})$ is the partial derivative of the Green's function between scatterer (i) and receiver $\mathbf{x}_R$ evaluated along the m-direction at $\mathbf{x}_R$. Equations 7-10 can therefore be used to solve a similar inverse problem to that in equation 6, to obtain the total wavefield from source $\mathbf{x}_S$ to receiver $\mathbf{x}_R$ when dipole or derivative Green's functions are used.

Since analytical Green's function formulae are available in all three dimensions, the calculation of the impulse response between two points is straightforward in 1D, 2D and 3D, as monopole and dipole (derivative) Green's functions can easily be calculated using

analytic formulae (see Appendix A). Figure 2 shows the results of modelling monopole (black solid curves) and dipole (dark gray dashed curves) Green's functions in one, two and three dimensions, with and without a source wavelet of central frequency 10 Hz: while the shape of the analytical Green's functions (Figures 2(a), 2(c), 2(e)) looks somewhat odd, realistic-looking seismograms (Figures 2(b), 2(d), 2(f)) are obtained when the analytical Green's functions are convolved with a wavelet (Figures 2(g) and 2(h)). In this example, a total of 256 frequencies were evaluated in the range 0.39-100 Hz in a medium of uniform velocity 1000 m s^{-1}, and for a source-receiver distance of 200 m. As expected, the arrival times in the monopole Green's functions peak at 0.2 s, while the analytical dipole Green's functions correctly reconstruct the spatial derivatives of the monopole signals (cfr. analytical derivatives obtained using the formulae in Appendix A and numerical derivatives obtained using a finite-difference approximation in Figures 2(b), 2(d) and 2(f)).

CODE DESCRIPTION

The Foldy acoustic modelling code *model_gfs_p_scat_acoust.m* that goes along with this paper is a well commented MATLAB script that models direct and scattered wavefields generated by monopole and dipole sources of volume injection and volume injection rate, recorded by monopole and dipole receivers. The code uses the analytical Green's function formulae in Appendix A to compute the impulse response of a medium of constant velocity c, with the option of applying a Ricker wavelet of a certain central frequency as source signature. In the absence of scatterers, the impulse response is evaluated only using the Green's function formulae in Appendix A; when scatterers are present, the code uses the above theory of multiple scattering developed by Foldy (1945) to compute the scattered part of the wavefield.

The code consists of a main MATLAB function and a number of sub-functions that work in combination:

- *model_gfs_p_scat_acoust.m*: the main modelling function, models direct and scattered acoustic pressure Green's functions in a homogeneous acoustic medium in the frequency domain, by applying the equations listed in the previous section.

- *acoustic_p_gfs_direct_f.m*: models direct Green's functions in a homogeneous acoustic medium in the frequency domain. These Green's functions are fed into *model_gfs_p_scat_acoust.m* to evaluate the total wavefield through the medium.

- *rickerwavl_time.m*: computes a Ricker wavelet of any desired central frequency f_c. The length of the wavelet (in seconds) is given by

$$\frac{n_t}{2f_{max}} \,, \tag{11}$$

  where f_{max} is the maximum modelled frequency and n_t is the nearest integer (towards infinity) to the ratio

$$\frac{2f_{max}}{f_c} \,. \tag{12}$$

- *centerfreqs.m*: creates a centred frequency spectrum from the one-sided spectrum obtained from modelling.

The outputs can be given in either or both of the frequency and time domains. If scattering is included, the wavefields are given as the sum of the direct and scattered wavefields (total wavefield), with the option of including separate direct and/or scattered wavefields in the output. Standard output includes a vector of the actual frequency/time samples for which output values are given, and the actual Ricker wavelet used if a source wavelet is applied.

APPLICATION TO SEISMIC INTERFEROMETRY

Seismic interferometry is a relatively new field of research in seismology which has been gaining increasing importance since its mathematical basis was derived early in this millennium. Although early results were obtained from laboratory experiments which used ultrasonic and thermal noise (Lobkis and Weaver, 2001; Weaver and Lobkis, 2001), the application of this technique currently spans a variety of fields, as interferometric theory may be equally applied to acoustic, elastic, electromagnetic, seismoelectric and electrokinetic wavefields. The term *seismic interferometry* refers to a set of methods of Green's function construction through cross-correlation (Wapenaar, 2004; van Manen et al., 2005, 2006; Wapenaar and Fokkema, 2006), convolution (Slob et al., 2007; Slob and Wapenaar, 2007) or deconvolution (Vasconcelos and Snieder, 2008a,b; Wapenaar et al., 2008; Wapenaar and van der Neut, 2010; Wapenaar et al., 2011; Minato et al., 2011) of seismic wavefields. Inter-receiver interferometry by cross-correlation uses a boundary of seismic sources (active sources such as dynamite or passive sources such as microseisms) to construct the Green's function between pairs of receivers located within the boundary as though one of the receivers had actually been a source that was recorded by the other receiver (Figure 3). This has important implications in the study of the Earth's properties, as new information about the medium of propagation can be obtained without directly recording the wavefield propagating between the two receiver locations (which would otherwise require a source to be placed at $\mathbf{x}_A$ in Figure 3). Within the Earth sciences, the application of seismic interferometry ranges from industrial exploration to crustal seismology and volcano monitoring: all of these applications take advantage of the fact that, in its various forms, seismic interferometry provides either new or more accessible information about the medium of propagation by converting receivers into virtual (imagined) sources of seismic energy, and vice-versa. This method

has been applied to image regional and continental scale seismic velocity structures (Sabra et al., 2005; Shapiro et al., 2005), for volcano or earthquake monitoring (Sens-Schönfelder and Wegler, 2006; Wegler and Sens-Schönfelder, 2007; Brenguier et al., 2007, 2008a,b), for industrial imaging (Bakulin and Calvert, 2004, 2006; Bakulin et al., 2007), noise removal (Curtis et al., 2006; Dong et al., 2006; Halliday et al., 2007, 2008, 2010; Halliday and Curtis, 2008, 2009b; Duguid et al., 2011), and to model synthetic waveforms (van Manen et al., 2005, 2006, 2007; Halliday et al., 2012).

Interferometry is a good area to test and demonstrate the Foldy code as it is a field in rapid development where new algorithms are being developed monthly (for reviews see Curtis et al. (2006), Wapenaar et al. (2010a,c), Galetti and Curtis (2012)). Because it is exact, the Foldy method of acoustic wavefield modelling provides a good method to test these new algorithms. Acoustic interferometric modelling formulae using wavefield cross-correlation or convolution have so far been derived by van Manen et al. (2005) and Wapenaar and Fokkema (2006) in the inter-receiver case, by Curtis et al. (2009) in the inter-source case, and by Curtis and Halliday (2010) in the source-receiver case. Further interferometric theory that uses deconvolution or multi-dimensional deconvolution of wavefields has been derived by Vasconcelos and Snieder (2008a), Vasconcelos and Snieder (2008b), Wapenaar et al. (2008), Minato et al. (2011) and Wapenaar et al. (2011). Because all of these formulae require traces from many combinations of boundary sources or receivers to be added or inverted using either cross-correlation, convolution or deconvolution, any error present in the modelled data will propagate across subsequent operations. As a consequence, although the formulae are exact, the practical results of applying seismic interferometry may not be as accurate as the theory predicts.

In the following sections, we show how synthetic data produced with our Foldy MAT-

LAB modelling code can be used to test the theory of inter-receiver interferometry. In the first example, the results of interferometry performed using exact and approximate interferometric formulae (see equations 13-14) are compared. In the second example, we use both the Foldy method and a finite-difference code to model signals from a boundary of sources to two central receivers. By performing interferometry with both datasets, we are then able to estimate the size of the errors produced by the two modelling schemes and to evaluate how errors in the modelling propagate through subsequent operations on the data. The code package also includes examples of inter-source and source-receiver interferometry which use similar geometries to those presented in the following examples.

Inter-receiver interferometry example

Classical inter-receiver interferometry uses a boundary of seismic sources to construct the wavefield that would propagate between the locations of two receivers within the medium of propagation. This is done by cross-correlating the traces recorded at the two receivers from each source on the boundary, and stacking (summing) all of those cross-correlations over the source positions. The result is a two-sided signal, each side representing energy travelling between the two receivers in one or other of the opposite directions. In mathematical form, this process can be represented by the following formula, given in the frequency domain where cross-correlation corresponds to a product when the complex conjugate of one of the factors is taken first (Wapenaar and Fokkema, 2006):

$$\begin{aligned} & G(\mathbf{x}_B, \mathbf{x}_A, \omega) - G^*(\mathbf{x}_B, \mathbf{x}_A, \omega) \\ &= \int_S \frac{1}{\rho(\mathbf{x})} \left[(\partial_j G(\mathbf{x}_B, \mathbf{x}, \omega))\, G^*(\mathbf{x}_A, \mathbf{x}, \omega) \right. \\ &\quad \left. - G(\mathbf{x}_B, \mathbf{x}, \omega)\, (\partial_j G^*(\mathbf{x}_A, \mathbf{x}, \omega)) \right] n_j \, \mathrm{d}S \, . \end{aligned} \tag{13}$$

Here, $\rho(\mathbf{x})$ is the density of the medium at $\mathbf{x}$, the superscript star * denotes complex conjugation in the frequency domain (equivalent to time-reversal in the time domain, if applied to all terms in the Fourier transform of a time series), ∂_j represents partial differentiation in the x_j-direction with respect to the source coordinate $\mathbf{x}$, n_j is the component of the boundary normal along the x_j-direction, and G and $\partial_j G$ represent Green's functions as responses to monopole and dipole sources. Einstein's summation convention applies for repeated indices and the integral over boundary S ensures summation over all boundary sources is performed.

By assuming a high frequency regime, that the surrounding surface of sources S is a sphere with very large radius, and that no energy scatters back through S once it has left, equation 13 can be simplified using the Sommerfield radiation conditions to eliminate the derivatives, giving (Wapenaar and Fokkema, 2006):

$$\begin{aligned} & G(\mathbf{x}_B, \mathbf{x}_A, \omega) - G^*(\mathbf{x}_B, \mathbf{x}_A, \omega) \\ & \approx \quad -\frac{2\iota\omega}{\rho c} \int\limits_S G(\mathbf{x}_B, \mathbf{x}, \omega) G^*(\mathbf{x}_A, \mathbf{x}, \omega)\, \mathrm{d}S \;, \end{aligned} \tag{14}$$

where c is the propagation velocity of the medium and ι is the imaginary unit. The result of either of equations 13 and 14 is a two sided signal, at positive and negative times: the causal (positive-time) part of the signal represents the Green's function between $\mathbf{x}_A$ and $\mathbf{x}_B$, while the acausal (negative-time) part of the signal represents the negative of the Green's function between $\mathbf{x}_A$ and $\mathbf{x}_B$ (or equivalently, the negative of the Green's function travelling between $\mathbf{x}_B$ and $\mathbf{x}_A$, by acoustic source-receiver reciprocity). Both formulae assume positive volume injection sources are used, as indicated in Wapenaar and Fokkema (2006).

In practical applications, where continuous source boundaries are not available, the integration factor in equations 13 and 14 can be discretised using a summation over M

sources, giving

$$\begin{aligned} & G(\mathbf{x}_B, \mathbf{x}_A, \omega) - G^*(\mathbf{x}_B, \mathbf{x}_A, \omega) \\ \approx & \sum_{k=1}^{M} \left\{ \frac{1}{\rho(\mathbf{x}_k)} \left[(\partial_j G(\mathbf{x}_B, \mathbf{x}_k, \omega)) \, G^*(\mathbf{x}_A, \mathbf{x}_k, \omega) \right. \right. \\ & \left. \left. -G(\mathbf{x}_B, \mathbf{x}_k, \omega) \, (\partial_j G^*(\mathbf{x}_A, \mathbf{x}_k, \omega)) \right] n_j \, \mathrm{d}S_k \right\} \end{aligned} \tag{15}$$

in place of equation 13, and

$$\begin{aligned} & G(\mathbf{x}_B, \mathbf{x}_A, \omega) - G^*(\mathbf{x}_B, \mathbf{x}_A, \omega) \\ \approx & -\frac{2\iota\omega}{\rho c} \sum_{k=1}^{M} \{ G(\mathbf{x}_B, \mathbf{x}_k, \omega) G^*(\mathbf{x}_A, \mathbf{x}_k, \omega) \, \mathrm{d}S_k \} \end{aligned} \tag{16}$$

in place of equation 14, where $\mathrm{d}S_k$ is the source sampling interval acting as an extra weighting factor for each source k. Equations 15 and 16 are normally implemented when transient sources at known positions are used for interferometry, and their application is demonstrated in the following examples (and in all of the other examples in the code package).

An example of the use of inter-receiver interferometry to construct the Green's function between two points within a circular boundary of sources (Figure 4) is shown in Figure 5. In this example we highlight the difference in the results of interferometry when the exact interferometric formula including both monopolar and dipolar sources in equation 15 (a discretised version of equation 13) and the approximate interferometric formula involving only monopolar sources in equation 16 (a discretised version of equation 14) are used. As expected, while the trace constructed using the exact interferometric formula in equation 15 (light gray dot-dashed) perfectly matches the true Green's function (black solid), the trace constructed using the approximate formula in equation 16 (dark gray dashed) presents small errors which are due to the approximation conditions not being completely satisfied (i.e., the radius of the circle has a finite size). The latter also contains a number of artefacts that

are non-physical and stationary with respect to source position (e.g., the event at ∼0.12 s). Each of these arrivals is the result of cross-correlation of the scattered monopole wavefields to A and B, and its amplitude is proportional to the energy scattered by the diffractor that produced it (Snieder et al., 2008; Wapenaar et al., 2010b). For the geometry in Figure 4, each scatterer (i) contributes a non-physical arrival at time

$$t_{(i)} = \left| \frac{|\mathbf{x}_A - \mathbf{x}_{(i)}| - |\mathbf{x}_B - \mathbf{x}_{(i)}|}{c} \right| , \tag{17}$$

where c is the velocity of the medium and $\mathbf{x}_A$, $\mathbf{x}_B$ and $\mathbf{x}_{(i)}$ are the positions of receiver A, receiver B and scatterer (i), respectively. For the geometry shown in Figure 4 and a background velocity of 1000 m s^{-1}, non-physical arrivals of this origin are expected at ∼0.03 s, ∼0.12 s and ∼0.20 s. Notice that, with the exception of the non-physical arrival at ∼0.12 s, most of the errors incurred by using equation 16 are so tiny that the modelling code must be extremely accurate to detect them and hence to test the severity of the approximation.

Foldy vs. FD modelling example

As outlined in the Introduction, the main advantage of the Foldy method over grid-based schemes such as finite-differences is the fact that it produces an exact construction of direct and scattered events. Since modelling errors can be neglected, any error in the outputs of an algorithm can be attributed to errors in the theory itself rather than to the modelling method. In this section, we show how errors in modelling may propagate across any further operation (e.g. cross-correlation) that is performed on the modelled data.

We used seismic interferometry to construct the Green's function between receivers A and B by using the signals produced by a circular boundary of sources (Figure 6). We produced two synthetic datasets using first our Foldy MATLAB code, and second the

2D finite-difference (FD) modelling code *fdelmodc* (courtesy of Jan Thorbecke, TU Delft). A grid-spacing of 1 m and a time-step of 0.5 ms were used in the FD modelling. In order to keep the two datasets as consistent as possible, scatterers were not included, only monopole volume-injection sources were used, and for both modelling codes interferometry was performed using the approximate formula in equation 16.

The reference Green's functions between A and B, modelled using the two methods, are shown in Figure 7. As illustrated by Thorbecke and Draganov (2011) in a similar experiment, the two Green's functions are perfectly overlapping, with a difference in the peak amplitude of less than 0.02%. However, when the Green's function between A and B is created using seismic interferometry, errors in the interferometric Green's function constructed from the FD data become more visible (Figure 8). Since the FD interferometric trace was constructed using the approximate Green's function formula, we are not able to determine whether the errors are caused by compounded effects of small imperfections in the modelled data, or by interferometry itself. In contrast, the Green's function constructed from the Foldy-modelled data closely matches the true Green's function. After observing similar effects in the previous example, we can safely conclude that any error in the interferometric Green's function in this case is due to the use of the approximate formula in equation 16, and not to the use of the Foldy code.

Finally, note that because it does not require a grid, in some cases the Foldy method may be faster than traditional FD modelling. In the above examples, the computation of the Green's functions from all sources to the two receivers took ∼352 seconds with *fdelmodc* and ∼4.7 seconds with *model_gfs_p_scat_acoust* on a Quad-Core AMD Opteron processor with CPU running at 2.21 GHz. This increase in efficiency may also contribute to more rigorous testing (on more cases/scenarios) of novel algorithms in future.

CONCLUSIONS

The ability to model exact data is an important requirement when testing new theory and algorithms in acoustics, seismics and seismology. At present, grid-based modelling schemes allow the user to produce synthetic seismograms for wavefields propagating through simple to very complex media. However, both time and space-domain discretization in such modelling schemes introduce errors that may propagate inside any subsequent operation that is performed on the synthetic data. On the other hand, analytical solutions to the wave equation are not subject to numerical dispersion errors and therefore provide exact results (to machine precision).

In this article, we presented a MATLAB code that uses analytical solutions to the wave equation in 1D, 2D and 3D to calculate Green's functions in multiply-scattering media. Although it is currently designed to work in the acoustic regime and to output monopole or dipole pressure responses, the theory behind the code could easily be transferred to an elastic modelling scheme. For example, this is possible provided that the scattering amplitudes used account for conversions between modes (e.g., P- and S-wave modes, or higher order surface wave modes). In the case of surface waves, we have also used a modified form of the 2D acoustic code that takes the dispersive nature of surface waves into account, and have found this is a quick and efficient way to model scattered surface waves.

In any case, because it is fast, exact and virtually error-free, this code may be an ideal choice when a synthetic dataset is needed to test the validity of new algorithms using simple geometries. If the theory in the algorithm is valid, one can then safely move on to more complex geometries that require grid-based modelling methods, or to real data tests and applications.

ACKNOWLEDGEMENTS

We thank Giovanni Angelo Meles (University of Edinburgh), Roel Snieder (Colorado School of Mines) and Dirk-Jan van Manen (Schlumberger) for advice during the creation of the Foldy modelling code, and Joe Dellinger, Kasper van Wijk and Jan Thorbecke for their constructive reviews, which helped improve this paper. The finite-difference dataset used in the interferometry example in Figures 7 and 8 was created using the *fdelmodc* code written by Jan Thorbecke at TU Delft. Finally, we thank the Natural Environment Research Council (NERC) and Schlumberger for supporting this research and granting us permission to publish.

APPENDIX A

ANALYTIC MONOPOLE AND DIPOLE GREEN'S FUNCTIONS

The monopole Green's function (impulse response) in a medium with constant velocity c satisfies the following equation in the frequency domain (the *Helmholtz equation*):

$$\nabla^2 G(\mathbf{x}, \mathbf{x}_0, \omega) + k^2 G(\mathbf{x}, \mathbf{x}_0, \omega) = -\delta(\mathbf{x} - \mathbf{x}_0) \ , \tag{A-1}$$

where $G(\mathbf{x}, \mathbf{x}_0, \omega)$ is the Green's function at location $\mathbf{x}$ due to a source at location $\mathbf{x}_0$, k is the wavenumber (which satisfies $k = \omega/c$, where ω is angular frequency), and the term $\delta(\mathbf{x} - \mathbf{x}_0)$ represents the source defined as a spatio-temporal impulse (delta function) acting at location $\mathbf{x}_0$ at time $t = 0$. The Helmholtz equation can be solved for the Green's function in N dimensions, and full derivations in one, two or three dimensions can be found in Snieder (2009). The solution to the Helmholtz equation is given in one dimension by

$$\begin{aligned} G^{1D}(x, x_0) &= -\frac{\iota}{2k} e^{-\iota k|x - x_0|} \\ &= -\frac{1}{2k} e^{-\iota\left(k|x - x_0| - \frac{\pi}{2}\right)} \ , \end{aligned} \tag{A-2}$$

in two dimensions by

$$G^{2D}(\mathbf{x}, \mathbf{x}_0) = -\frac{\iota}{4} H_0^{(2)}(k|\mathbf{x} - \mathbf{x}_0|) \ , \tag{A-3}$$

in two dimensions (far-field case) by

$$\begin{aligned} G^{2D\text{-}far}(\mathbf{x}, \mathbf{x}_0) &= -\frac{\iota}{4} e^{-\iota\left(k|\mathbf{x} - \mathbf{x}_0| - \frac{\pi}{4}\right)} \sqrt{\frac{2}{\pi k|\mathbf{x} - \mathbf{x}_0|}} \\ &= -\frac{1}{4} e^{-\iota\left(k|\mathbf{x} - \mathbf{x}_0| - \frac{3\pi}{4}\right)} \sqrt{\frac{2}{\pi k|\mathbf{x} - \mathbf{x}_0|}} \ , \end{aligned} \tag{A-4}$$

and in three dimensions by

$$G^{3D}(\mathbf{x}, \mathbf{x}_0) = \frac{1}{4\pi} \frac{e^{-\iota k|\mathbf{x} - \mathbf{x}_0|}}{|\mathbf{x} - \mathbf{x}_0|} \ , \tag{A-5}$$

where $H_0^{(2)}$ is the Hankel function of the second kind and order 0, and the imaginary unit $\iota = \sqrt{-1}$ has been taken inside the exponential term in the second line of equations A-2 and A-4.

Dipole Green's functions may be obtained from spatial differentiation of equations A-2-A-5 and are given by

$$\partial G^{1D}(x, x_0) = -\iota k G^{1D}(x, x_0) \tag{A-6}$$

in one dimension, by

$$\partial_m G^{2D}(\mathbf{x}, \mathbf{x}_0) = \frac{\iota k}{4} \cos(\phi_m) H_1^{(2)}(k|\mathbf{x} - \mathbf{x}_0|) \ , \tag{A-7}$$

in two dimensions, by

$$\partial_m G^{2D\text{-}far}(\mathbf{x}, \mathbf{x}_0) = -G^{2D\text{-}far}(\mathbf{x}, \mathbf{x}_0) \cos(\phi_m) \left[\iota k + \frac{1}{2|\mathbf{x} - \mathbf{x}_0|}\right] \ , \tag{A-8}$$

in two dimensions (far-field case), and by

$$\partial_m G^{3D}(\mathbf{x}, \mathbf{x}_0) = -G^{3D}(\mathbf{x}, \mathbf{x}_0) \cos(\phi_m) \left[\iota k + \frac{1}{|\mathbf{x} - \mathbf{x}_0|}\right] \ , \tag{A-9}$$

in three dimensions. $H_1^{(2)}$ is the Hankel function of the second kind and order 1, and the term $\cos(\phi_m)$ is the direction cosine of the receiver position $\mathbf{x}$ with respect to the source location $\mathbf{x}_0$ along the m-direction, i.e., the cosine of the angle between vector $\mathbf{x} - \mathbf{x}_0$ and the m-direction. Note that all above equations assume the exponential term in the Fourier transform from frequency to time domain to be $e^{\iota\omega t}$, which is the sign convention used by MATLAB (as opposed to $e^{-\iota\omega t}$, which is more usual in Geophysics, for example).

APPENDIX B

SCATTERING AMPLITUDE IN D-DIMENSIONS

For a certain distribution of N isotropic point scatterers, the scattering amplitude $A^{(i)}$ of scatterer (i) located at $\mathbf{x}^{(i)}$ is a complex quantity that relates the total wavefield $\Psi_0(\mathbf{x}^{(i)})$ incident on the scatterer to the scattered wavefield $\Psi_S(\mathbf{x})$ measured at $\mathbf{x}$, according to

$$\Psi_S(\mathbf{x}) = \Psi_0(\mathbf{x}^{(i)}) A^{(i)} G(\mathbf{x}, \mathbf{x}^{(i)}) \,, \tag{B-1}$$

where $G(\mathbf{x}, \mathbf{x}^{(i)})$ is the Green's function between $\mathbf{x}^{(i)}$ and $\mathbf{x}$. As shown by Snieder (1999), the scattering amplitude contains the superposition of all possible multiple scattering interactions with the same scatterer and, since scattering is assumed to be isotropic, is independent of the angle of incidence.

The real and imaginary parts of the scattering amplitude are related via the optical theorem (generally, an optical theorem describes the conservation of energy between a wave incident on a scattering object and the resulting wave scattered by that object). In simple acoustic media with uniform background velocity, the relationship between the real and imaginary part of the scattering amplitude can be derived by equating the total energy loss for unit incident wavefield (the so-called *total cross-section* Ω_T) to the total scattered energy (the so-called *scattering cross-section* Ω_S). This approach assumes that no energy is lost to anelastic attenuation, hence the energy loss of the incident wavefield is due to scattering alone.

In two dimensions, the total and scattering cross-sections are given respectively by (Groenenboom and Snieder, 1995)

$$\Omega_T = -\frac{\Im(A)}{k} \tag{B-2}$$

and

$$\Omega_S = \frac{|A|^2}{4k} \,, \tag{B-3}$$

where the latter expression is obtained by using the far-field Green's function (equation A-4) to get Ψ_S in equation B-1 and integrating the power of the scattered field $|\Psi_S|^2 = \Psi_S \Psi_S^*$ over 2π. Using a similar approach, expressions similar to those in the above equations can be derived in one and three dimensions, and by equating the total and scattering cross-sections the relationships between the real and imaginary parts of the scattering amplitude can be obtained in one, two and three dimensions (Snieder, 1999):

$$\Re(A) = \pm \begin{cases} \left(-\Im(A)\left[2k + \Im(A)\right]\right)^{1/2} & \text{in 1D} \\ \left(-\Im(A)\left[4 + \Im(A)\right]\right)^{1/2} & \text{in 2D} \\ \left(-\Im(A)\left[\dfrac{4\pi}{k} + \Im(A)\right]\right)^{1/2} & \text{in 3D} \end{cases} \tag{B-4}$$

These expressions impose the following constraints on the value of the imaginary part of the scattering amplitude:

$$\begin{aligned} -2k \leq \Im(A) \leq 0 \quad & \text{in 1D} \\ -4 \leq \Im(A) \leq 0 \quad & \text{in 2D} \\ -\frac{4\pi}{k} \leq \Im(A) \leq 0 \quad & \text{in 3D} \end{aligned} \tag{B-5}$$

The relationships between the real and imaginary components of A are of particular importance as they ensure that the scattering strength of each scatterer satisfies the requirement of energy conservation. Optical theorems for more complex scattering media also exist (Halliday and Curtis, 2009a; Douma et al., 2011; Wapenaar and Douma, 2012) and can be applied to obtain a correct estimate of the scattering amplitude. However, the details of these theorems will not be discussed here as their application is beyond the scope of our simple modelling code.

REFERENCES

Bakulin, A., and R. Calvert, 2004, Virtual source: new method for imaging and 4D below complex overburden: SEG Technical Program Expanded Abstracts, **23**, 2477–2480.

———, 2006, The virtual source method: Theory and case study: Geophysics, **71**, SI139–SI150.

Bakulin, A., A. Mateeva, K. Mehta, P. Jorgensen, J. Ferrandis, I. S. Herhold, and J. Lopez, 2007, Virtual source applications to imaging and reservoir monitoring: The Leading Edge, **26**, 732–740.

Berkhout, A. J., and C. P. A. Wapenaar, 1989, One-way versions of the Kirchhoff Integral: Geophysics, **54**, 460–467.

Brenguier, F., M. Campillo, C. Hadziioannou, N. M. Shapiro, R. M. Nadeau, and E. Larose, 2008a, Postseismic Relaxation Along the San Andreas Fault at Parkfield from Continuous Seismological Observations: Science, **321**, 1478–1481.

Brenguier, F., N. M. Shapiro, M. Campillo, V. Ferrazzini, Z. Duputel, O. Coutant, and A. Nercessian, 2008b, Towards forecasting volcanic eruptions using seismic noise: Nature Geosci, **1**, 126–130.

Brenguier, F., N. M. Shapiro, M. Campillo, A. Nercessian, and V. Ferrazzini, 2007, 3-D surface wave tomography of the Piton de la Fournaise volcano using seismic noise correlations: Geophys. Res. Lett., **34**, L02305.

Cassereau, D., and M. Fink, 1993, Focusing with plane time-reversal mirrors: An efficient alternative to closed cavities: The Journal of the Acoustical Society of America, **94**, 2373–2386.

Curtis, A., P. Gerstoft, H. Sato, R. Snieder, and K. Wapenaar, 2006, Seismic interferometry—turning noise into signal: The Leading Edge, **25**, 1082–1092.

Curtis, A., and D. Halliday, 2010, Source-receiver wave field interferometry: Physical Review E, **81**, 046601.

Curtis, A., H. Nicolson, D. Halliday, J. Trampert, and B. Baptie, 2009, Virtual seismometers in the subsurface of the Earth from seismic interferometry: Nature Geosci, **2**, 700–704.

Dong, S., R. He, and G. T. Schuster, 2006, Interferometric predcition and least squares subtraction of surface waves: SEG Technical Program Expanded Abstracts, **25**, 2783–2786.

Douma, H., I. Vasconcelos, and R. Snieder, 2011, The reciprocity theorem for the scattered field is the progenitor of the generalized optical theorem: The Journal of the Acoustical Society of America, **129**, 2765–2771.

Duguid, C., D. Halliday, and A. Curtis, 2011, Source-receiver interferometry for seismic wavefield construction and ground-roll removal: The Leading Edge, **30**, 838–843.

Fink, M., 2006, Time-reversal acoustics in complex environments: Geophysics, **71**, SI151–SI164.

Fink, M., and C. Prada, 2001, Acoustic time-reversal mirrors: Inverse Problems, **17**, R1.

Foldy, L. L., 1945, The Multiple Scattering of Waves. I. General Theory of Isotropic Scattering by Randomly Distributed Scatterers: Phys. Rev., **67**, no. 3-4, 107–119.

Galetti, E., and A. Curtis, 2012, Generalised receiver functions and seismic interferometry: Tectonophysics, **532-535**, 1–26.

Groenenboom, J., and R. Snieder, 1995, Attenuation, dispersion, and anisotropy by multiple scattering of transmitted waves through distributions of scatterers: The Journal of the Acoustical Society of America, **98**, 3482–3492.

Halliday, D., and A. Curtis, 2008, Seismic interferometry, surface waves and source distribution: Geophysical Journal International, **175**, 1067–1087.

———, 2009a, Generalized optical theorem for surface waves and layered media: Physical Review E, **79**, 056603.

———, 2009b, Seismic interferometry of scattered surface waves in attenuative media: Geophysical Journal International, **178**, 419–446.

———, 2010, An interferometric theory of source-receiver scattering and imaging: Geophysics, **75**, SA95–SA103.

Halliday, D., A. Curtis, and E. Kragh, 2008, Seismic surface waves in a suburban environment: Active and passive interferometric methods: The Leading Edge, **27**, 210–218.

Halliday, D., A. Curtis, and K. Wapenaar, 2012, Generalized PP+PS=SS from seismic interferometry: Geophysical Journal International, **189**, 1015–1024.

Halliday, D. F., A. Curtis, J. O. A. Robertsson, and D.-J. van Manen, 2007, Interferometric surface-wave isolation and removal: Geophysics, **72**, A69–73.

Halliday, D. F., A. Curtis, P. Vermeer, C. Strobbia, A. Glushchenko, D. van Manen, and J. Robertsson, 2010, Interferometric ground-roll removal: Attenuation of scattered surface waves in single-sensor data: Geophysics, **75**, SA15–SA25.

Lobkis, O. I., and R. L. Weaver, 2001, On the emergence of the Green's function in the correlations of a diffuse field: The Journal of the Acoustical Society of America, **110**, 3011–3017.

MathWorks, 2012, Systems of Linear Equations: `http://www.mathworks.co.uk/help/matlab/math/systems-of-linear-equations.html`. (Online; last accessed: 08 February 2013).

Minato, S., T. Matsuoka, T. Tsuji, D. Draganov, J. Hunziker, and K. Wapenaar, 2011, Seismic interferometry using multidimensional deconvolution and crosscorrelation for crosswell seismic reflection data without borehole sources: Geophysics, **76**, SA19–SA34.

Moldoveanu, N., L. Combee, M. Egan, G. Hampson, L. Sydora, and W. Abriel, 2007, Over/under towed-streamer acquisition: The Leading Edge, **26**, 41–58.

Sabra, K. G., P. Gerstoft, P. Roux, W. A. Kuperman, and M. C. Fehler, 2005, Surface wave tomography from microseisms in Southern California: Geophys. Res. Lett., **32**, L14311.

Sens-Schönfelder, C., and U. Wegler, 2006, Passive image interferometry and seasonal variations of seismic velocities at Merapi Volcano, Indonesia: Geophys. Res. Lett., **33**, L21302.

Shapiro, N. M., M. Campillo, L. Stehly, and M. H. Ritzwoller, 2005, High-Resolution Surface-Wave Tomography from Ambient Seismic Noise: Science, **307**, 1615–1618.

Slob, E., D. Draganov, and K. Wapenaar, 2007, Interferometric electromagnetic Green's functions representations using propagation invariants: Geophysical Journal International, **169**, 60–80.

Slob, E., and K. Wapenaar, 2007, Electromagnetic Green's functions retrieval by cross-correlation and cross-convolution in media with losses: Geophys. Res. Lett., **34**, L05307.

Snieder, R., 1988a, Large-Scale Waveform Inversions of Surface Waves for Lateral Heterogeneity 1. Theory and Numerical Examples: J. Geophys. Res., **93**, 12055–12065.

———, 1988b, Large-Scale Waveform Inversions of Surface Waves for Lateral Heterogeneity 2. Application to Surface Waves in Europe and the Mediterranean: J. Geophys. Res., **93**, 12067–12080.

———, 1999, Imaging and averaging in complex media, *in* Diffuse waves in complex media: Kluwer Academic Publishers, volume **531** *of* NATO Science Series - Series C: Mathematical and Physical Sciences, 405–454.

———, 2009, A Guided Tour of Mathematical Methods For the Physical Sciences, 2 ed.: Cambridge University Press.

Snieder, R., K. van Wijk, M. Haney, and R. Calvert, 2008, Cancellation of spurious arrivals

in Green's function extraction and the generalized optical theorem: Phys. Rev. E, **78**, no. 3, 036606.

Thorbecke, J. W., and D. Draganov, 2011, Finite-difference modeling experiments for seismic interferometry: Geophysics, **76**, H1–H18.

van Manen, D.-J., A. Curtis, and J. O. A. Robertsson, 2006, Interferometric modeling of wave propagation in inhomogeneous elastic media using time reversal and reciprocity: Geophysics, **71**, SI47–SI60.

van Manen, D.-J., J. O. A. Robertsson, and A. Curtis, 2005, Modeling of Wave Propagation in Inhomogeneous Media: Physical Review Letters, **94**, 164301.

———, 2007, Exact wave field simulation for finite-volume scattering problems: The Journal of the Acoustical Society of America, **122**, EL115–EL121.

Vasconcelos, I., P. Sava, and H. Douma, 2009, Wave-equation extended images via image-domain interferometry: SEG Technical Program Expanded Abstracts, **28**, 2839–2843.

———, 2010, Nonlinear extended images via image-domain interferometry: Geophysics, **75**, SA105–SA115.

Vasconcelos, I., and R. Snieder, 2008a, Interferometry by deconvolution: Part 1 – Theory for acoustic waves and numerical examples: Geophysics, **73**, S115–128.

———, 2008b, Interferometry by deconvolution: Part 2 – Theory for elastic waves and application to drill-bit seismic imaging: Geophysics, **73**, S129–141.

Wapenaar, C. P. A., 1993, Kirchhoff-Helmholtz downward extrapolation in a layered medium with curved interfaces: Geophysical Journal International, **115**, 445–455.

Wapenaar, K., 2004, Retrieving the Elastodynamic Green's Function of an Arbitrary Inhomogeneous Medium by Cross Correlation: Physical Review Letters, **93**, 254301.

Wapenaar, K., and H. Douma, 2012, A unified optical theorem for scalar and vectorial wave

fields: The Journal of the Acoustical Society of America, **131**, 3611–3626.

Wapenaar, K., D. Draganov, R. Snieder, X. Campman, and A. Verdel, 2010a, Tutorial on seismic interferometry: Part 1 – Basic principles and applications: Geophysics, **75**, 75A195–75A209.

Wapenaar, K., and J. Fokkema, 2006, Green's function representations for seismic interferometry: Geophysics, **71**, SI33–SI46.

Wapenaar, K., E. Ruigrok, J. van der Neut, and D. Draganov, 2011, Improved surface-wave retrieval from ambient seismic noise by multi-dimensional deconvolution: Geophys. Res. Lett., **38**, L01313.

Wapenaar, K., E. Slob, and R. Snieder, 2010b, On seismic interferometry, the generalized optical theorem, and the scattering matrix of a point scatterer: Geophysics, **75**, SA27–SA35.

Wapenaar, K., E. Slob, R. Snieder, and A. Curtis, 2010c, Tutorial on seismic interferometry: Part 2 – Underlying theory and new advances: Geophysics, **75**, 75A211–75A227.

Wapenaar, K., and J. van der Neut, 2010, A representation for Green's function retrieval by multidimensional deconvolution: The Journal of the Acoustical Society of America, **128**, EL366–EL371.

Wapenaar, K., J. van der Neut, and E. Ruigrok, 2008, Passive seismic interferometry by multidimensional deconvolution: Geophysics, **73**, A51–A56.

Weaver, R. L., and O. I. Lobkis, 2001, Ultrasonics without a Source: Thermal Fluctuation Correlations at MHz Frequencies: Physical Review Letters, **87**, 134301.

Wegler, U., and C. Sens-Schönfelder, 2007, Fault zone monitoring with passive image interferometry: Geophysical Journal International, **168**, 1029–1033.

LIST OF FIGURES

1 The total wavefield reaching a receiver at $\mathbf{x}_R$ from a source at $\mathbf{x}_S$, and scattered by a number of diffractors (e.g. $\mathbf{x}^{(i)}$, $\mathbf{x}^{(j)}$), is given by the sum of a direct term (dark gray solid arrow) and a multiply scattered term (sum of all of the black dashed arrows), as indicated in equation 1.

2 Examples of wavefield modelling in (a) 1D, (c) 2D and (e) 3D using analytical Green's function formulae. The medium has velocity 1000 m s^{-1} and the source-receiver distance is 200 m. A wavelet of central frequency 10 Hz (bottom panels: in time domain (g) and frequency domain (h)) is applied to the analytical Green's functions shown in the top-three left panels to give the corresponding seismograms in (b) 1D, (d) 2D and (f) 3D. Derivative Green's functions are calculated analytically within the code (light gray solid traces) and are compared to numerical derivatives (dark gray dashed traces) obtained by placing additional sources along the direction of differentiation and using finite-differences (Richardson's extrapolation) to calculate the derivative. The analytical derivatives obtained with the Foldy code perfectly match the numerical derivatives.

3 Schematic illustration of a typical geometry for correlational seismic interferometry. Two receivers (inverted triangles) are surrounded by a boundary of sources (explosions); at each source position, the boundary normal is denoted by $\hat{\mathbf{n}}$. The method of seismic interferometry uses one of the receivers (e.g. $\mathbf{x}_A$) as a 'virtual' (imagined) source, and constructs the signal (Green's function) as though this source was recorded by the other receiver (e.g. $\mathbf{x}_B$).

4 Geometry of numerical example with results in Figure 5: two receivers (inverted triangles) and three scatterers (empty circles) are surrounded by a circular boundary of sources (stars). Only every sixth source is shown for clarity.

5 True and (positive-time) interferometric traces from receiver A to receiver B in Figure 4 with four magnified panels. The light-gray dot-dashed trace, constructed using the exact interferometric formula in equation 15 (discretised version of equation 13), perfectly matches the true trace; the dark-gray dashed trace, constructed using the approximate interferometric formula in equation 16 (discretised version of equation 14), presents some errors which are due to the approximations in that formula. The arrival at $\sim$0.12 s on the monopole interferometry trace is non-physical, stationary with respect to the sources, and arises from the cross-correlation of scattered waves to A and B. Similarly, the error in the monopole interferometry trace shown in the top-left magnified panel is due to interference with a non-physical arrival of similar origin at $\sim$0.20 s.

6 Experimental geometry used to obtain results in Figures 7 and 8: two receivers (inverted triangles) are surrounded by a circular boundary of sources (stars). Only every sixth source is shown for clarity.

7 True traces from receiver A to receiver B in Figure 6 evaluated using the 2D analytic Green's function formula used in the Foldy method (black solid line), and a finite-difference method (gray dot-dashed line). The two traces overlap almost perfectly, and differences are only visible in the magnified panels.

8 True and (positive-time) interferometric traces from receiver A to receiver B. Because interferometry was performed using the approximate interferometric formula in equation 14, small errors are visible in the interferometric Green's functions. The errors are larger for the trace constructed using the finite-difference modelled data. Only the availability of the Foldy solution makes clear that these errors are not due to the monopole approximation in equation 14, but derive directly from the tiny finite-difference errors observed in Figure 7.

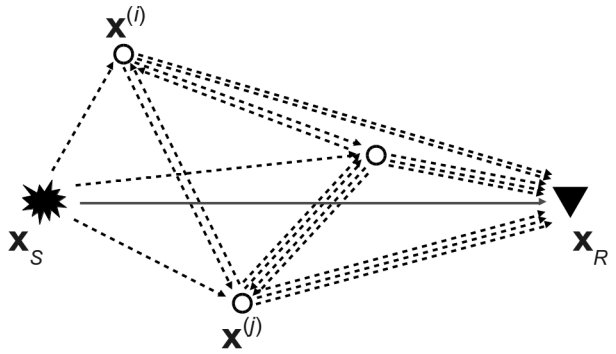

Figure 1: The total wavefield reaching a receiver at $\mathbf{x}_R$ from a source at $\mathbf{x}_S$, and scattered by a number of diffractors (e.g. $\mathbf{x}^{(i)}$, $\mathbf{x}^{(j)}$), is given by the sum of a direct term (dark gray solid arrow) and a multiply scattered term (sum of all of the black dashed arrows), as indicated in equation 1.

Galetti et al. (2012) –

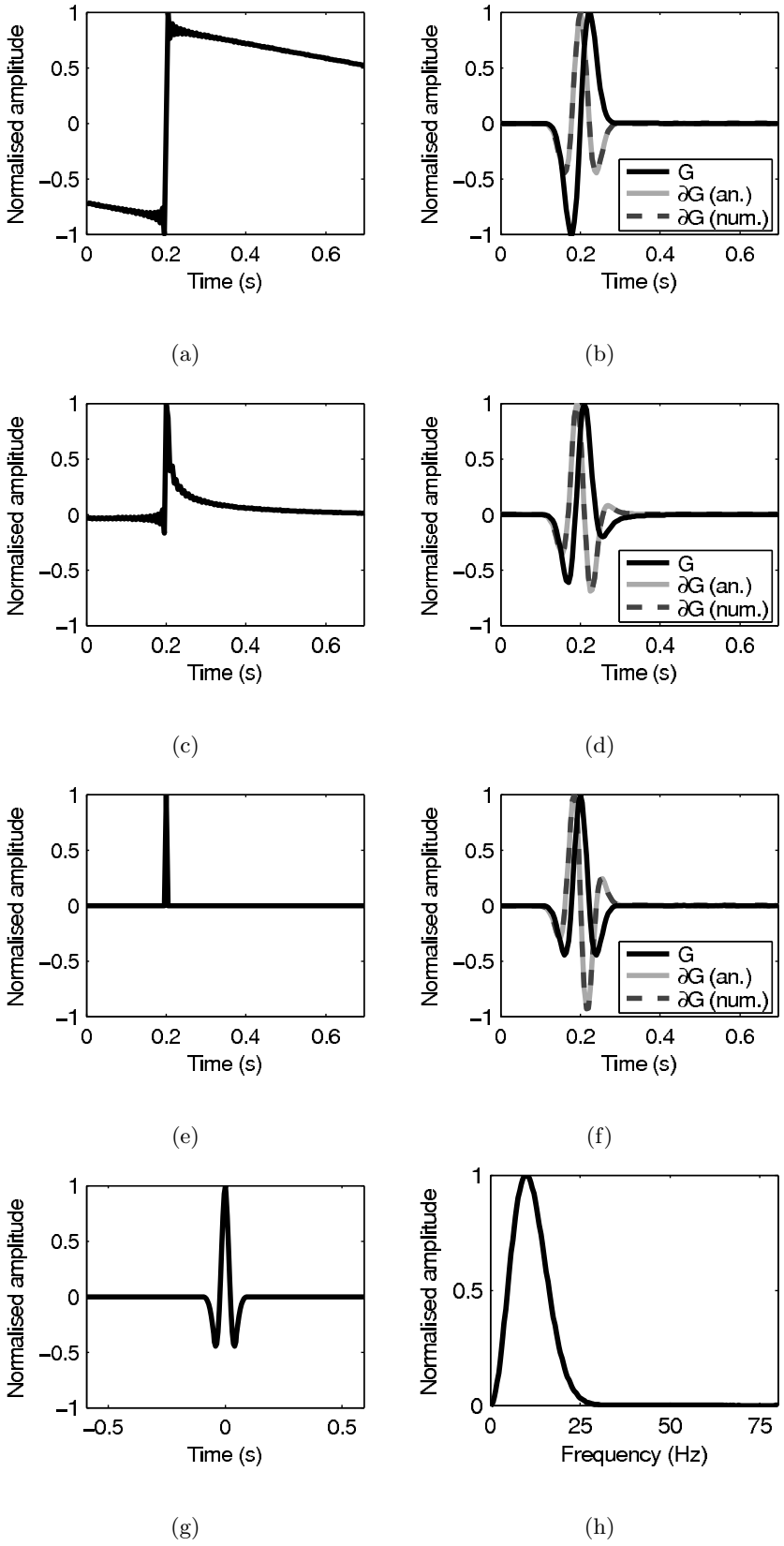

Figure 2: Examples of wavefield modelling in (a) 1D, (c) 2D and (e) 3D using analytical Green's function formulae. The medium has velocity 1000 m s^{-1} and the source-receiver

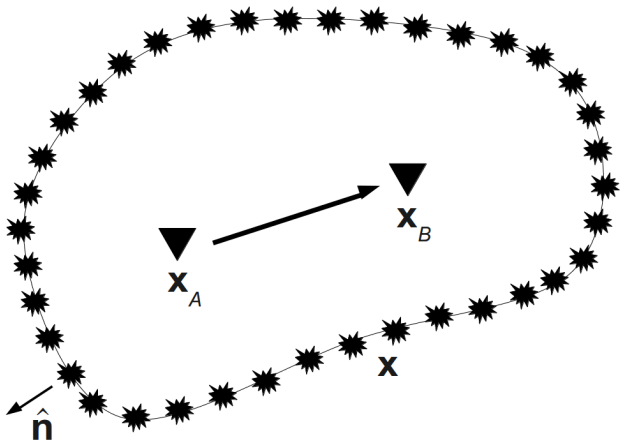

Figure 3: Schematic illustration of a typical geometry for correlational seismic interferometry. Two receivers (inverted triangles) are surrounded by a boundary of sources (explosions); at each source position, the boundary normal is denoted by $\hat{\mathbf{n}}$. The method of seismic interferometry uses one of the receivers (e.g. $\mathbf{x}_A$) as a 'virtual' (imagined) source, and constructs the signal (Green's function) as though this source was recorded by the other receiver (e.g. $\mathbf{x}_B$).

Galetti et al. (2012) –

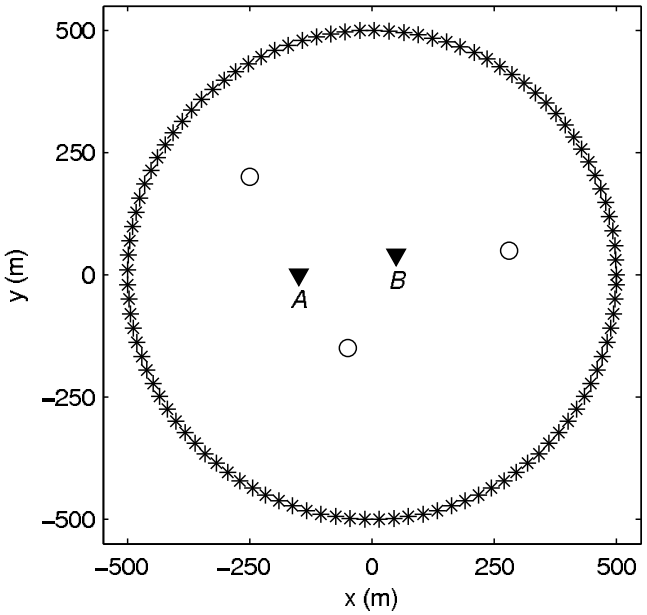

Figure 4: Geometry of numerical example with results in Figure 5: two receivers (inverted triangles) and three scatterers (empty circles) are surrounded by a circular boundary of sources (stars). Only every sixth source is shown for clarity.

Galetti et al. (2012) –

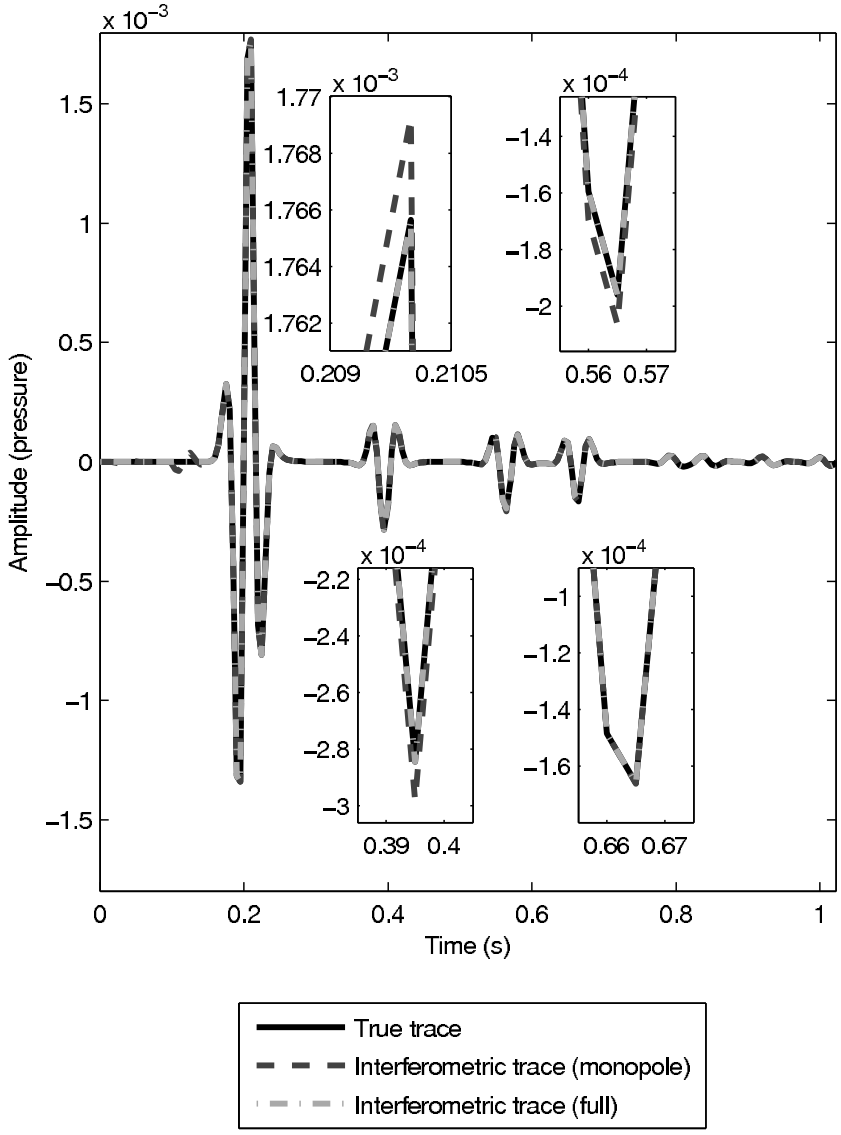

Figure 5: True and (positive-time) interferometric traces from receiver A to receiver B in Figure 4 with four magnified panels. The light-gray dot-dashed trace, constructed using the exact interferometric formula in equation 15 (discretised version of equation 13), perfectly matches the true trace; the dark-gray dashed trace, constructed using the approximate interferometric formula in equation 16 (discretised version of equation 14), presents some errors which are due to the approximations in that formula. The arrival at $\sim$0.12 s on the monopole interferometry trace is non-physical, stationary with respect to the sources, and arises from the cross-correlation of scattered waves to A and B. Similarly, the error in the

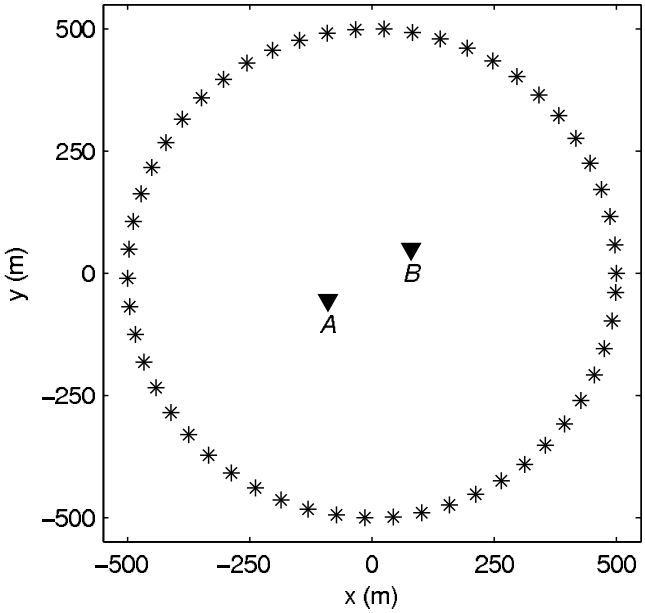

Figure 6: Experimental geometry used to obtain results in Figures 7 and 8: two receivers (inverted triangles) are surrounded by a circular boundary of sources (stars). Only every sixth source is shown for clarity.

Galetti et al. (2012) –

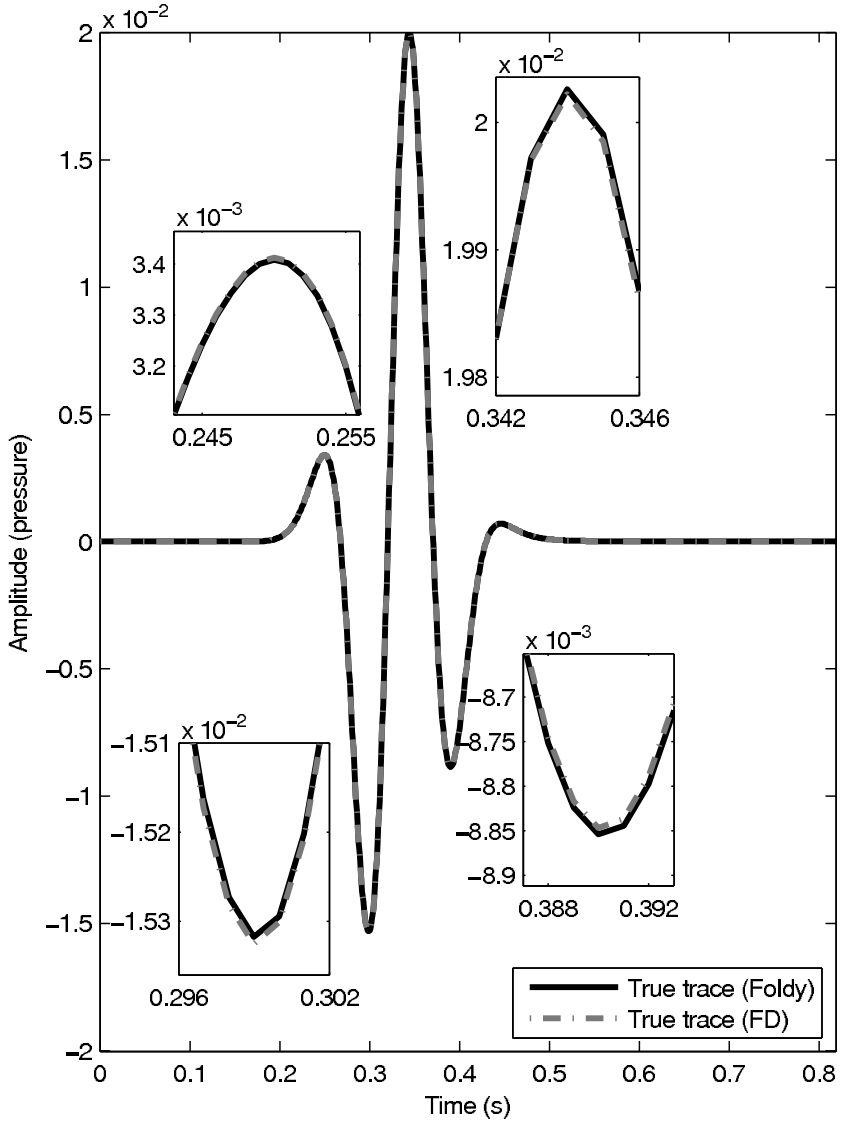

Figure 7: True traces from receiver A to receiver B in Figure 6 evaluated using the 2D analytic Green's function formula used in the Foldy method (black solid line), and a finite-difference method (gray dot-dashed line). The two traces overlap almost perfectly, and differences are only visible in the magnified panels.

Galetti et al. (2012) –

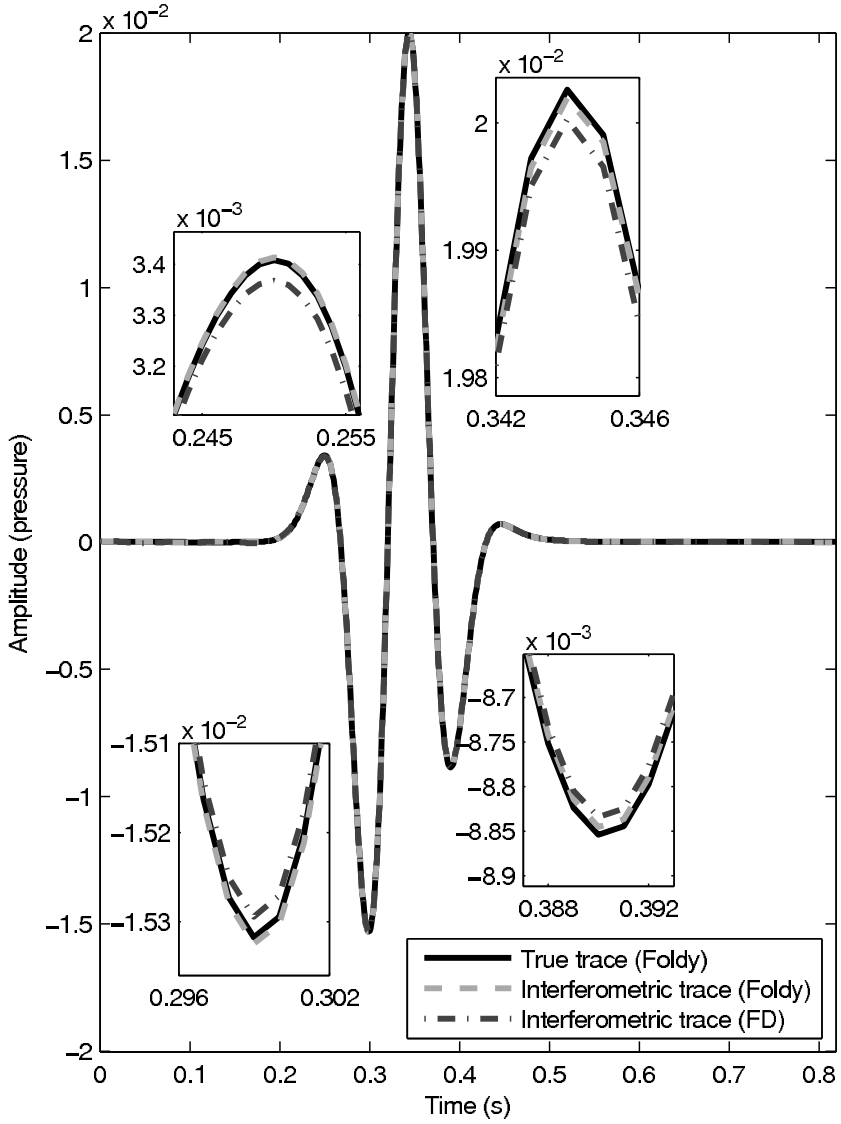

Figure 8: True and (positive-time) interferometric traces from receiver A to receiver B. Because interferometry was performed using the approximate interferometric formula in equation 14, small errors are visible in the interferometric Green's functions. The errors are larger for the trace constructed using the finite-difference modelled data. Only the availability of the Foldy solution makes clear that these errors are not due to the monopole approximation in equation 14, but derive directly from the tiny finite-difference errors observed in Figure 7.